Lattice Boltzmann simulations of contact line motion. II. Binary fluids

A. J. Briant and J. M. Yeomans
Department of Physics, Theoretical Physics, University of Oxford, 1 Keble Road, Oxford OX1 3NP, United Kingdom
(Received 26 July 2003; published 22 March 2004)

We investigate the applicability of a mesoscale modeling approach, lattice Boltzmann simulations, to the problem of contact line motion in one- and two-component two phase fluids. In this, the second of two papers, we consider binary systems. We show that the contact line singularity is overcome by diffusion which is effective over a length scale L about the contact line and derive a scaling form for the dependence of L on system parameters.

DOI: 10.1103/PhysRevE.69.031603 PACS number(s): 68.05.−n, 68.08.−p, 47.55.Kf

I. INTRODUCTION

In the preceeding paper of the same principal title [1], which we shall refer to as I, we investigated the way in which lattice Boltzmann simulations can be used to describe contact line motion in liquid-gas systems. We found that the diffuse nature of the interface in the model allowed movement of the contact line by evaporation and condensation of the surrounding fluid. We now undertake a similar investigation of contact line motion in binary systems. We find, in agreement with Jacqmin [2] and Chen *et al.* [3], a different slip mechanism: the relative diffusion of the two fluid components in the vicinity of the contact line. For a summary of the literature we refer the reader to the introduction in I and the conclusion of this paper.

In this paper we first summarize the extensions to the lattice Boltzmann scheme described in I needed to treat a binary system. We then describe how to implement wetting boundary conditions so that the equilibrium contact angle obtained in the simulations can be predicted using Cahn theory.

The algorithm is used to study the behavior of a sheared interface. We observe that diffuse interface effects are important within a length L of the contact line and give a scaling argument, backed by numerical results, for how L depends on system parameters, such as viscosity, surface tension and the diffusion constant. Our results differ from those obtained by other authors. In particular we find that diffusive effects do not increase as the contact line speed is reduced. We show that in the limit that corresponds to strictly immiscible fluids our data are consistent with the classical treatment which imposes a slip length to overcome the contact line singularity.

II. LATTICE BOLTZMANN MODEL

The free energy lattice Boltzmann model for one-component fluids is described in section II of I. We now consider a binary fluid with density n_A and n_B of components A and B, respectively. The total fluid density is defined by $n=n_A+n_B$ and the order parameter is the concentration $\phi=n_A-n_B$.

We consider a two dimensional square lattice with N_x and N_y sites in the x and y directions, respectively. The lattice sites are labeled by coordinates (i,j) with $i=1,2,3,\ldots,N_x$ and $j=1,2,3,\ldots,N_y$. The lattice spacing is Δx and we use nine velocity vectors (the so-called D2Q9 lattice). The velocity vectors are labeled by the subscript $\sigma=\mathbf{e}_{\sigma i}^2/c^2$, where $c=\Delta x/\Delta t$, the lattice speed. For $\sigma=1$ and 2 the label i runs from 1 to 4 (this label i is distinct from the coordinate i as clear from the context). The zero speed vector is labeled $\mathbf{e}_{0,0}$. To extend the lattice Boltzmann approach to a binary fluid an additional set of fields $g_{\sigma i}(\mathbf{x},t)$ are needed. These are related to the concentration by

$$\sum_{\sigma,i} g_{\sigma i}=\phi. \tag{1}$$

The $g_{\sigma i}(\mathbf{x},t)$ are evolved according to a lattice Boltzmann equation assuming a single non dimensional relaxation time τ_g:

$$g_{\sigma i}(\mathbf{x}+\mathbf{e}_{\sigma i}\Delta t,t+\Delta t)-g_{\sigma i}(\mathbf{x},t)=-\frac{1}{\tau_g}(g_{\sigma i}-g_{\sigma i}^{eq}). \tag{2}$$

$g_{\sigma i}^{eq}$ is a local equilibrium distribution. To gain an explicit representation of $g_{\sigma i}^{eq}$ we expand it as a power series in the local velocity:

$$g_{\sigma i}^{eq}=H_\sigma+K_\sigma e_{\sigma i\alpha}u_\alpha+J_\sigma u^2+Q_\sigma e_{\sigma i\alpha}e_{\sigma i\beta}u_\alpha u_\beta. \tag{3}$$

To impose the correct conservation laws for the order parameter the equilibrium distribution function is constrained by imposing

$$\sum_{\sigma,i} g_{\sigma i}^{eq}=\phi. \tag{4}$$

Higher order moments of $g_{\sigma i}^{eq}$ are chosen so that the continuum level equations correctly describe the dynamics of a binary fluid mixture. These constraints are

$$\sum_{\sigma i} g_{\sigma i}^{eq}e_{\sigma i\alpha}=\phi u_\alpha, \tag{5}$$

$$\sum_{\sigma i} g_{\sigma i}^{eq}e_{\sigma i\alpha}e_{\sigma i\beta}=\Gamma\mu\delta_{\alpha\beta}+\phi u_\alpha u_\beta, \tag{6}$$

where μ is the chemical potential and Γ is a constant related to the mobility. Equations (1)–(6), together with equations

I(2)–I(9) define the lattice Boltzmann scheme for a binary fluid. Possible values for the coefficients in I(5) and (3) are listed in the Appendix.

Performing a Chapman-Enskog expansion [4] shows that the algorithm leads to the continuity equation

$$\partial_t n + \partial_\alpha (n u_\alpha) = 0, \tag{7}$$

the Navier-Stokes equation

$$\begin{aligned}
&\partial_t (n u_\gamma) + \partial_\alpha (n u_\gamma u_\alpha) \\
&\quad = -\partial_\alpha P_{\alpha\gamma} + \nu \partial_\beta \Bigg[n \partial_\gamma u_\beta + n \partial_\beta u_\gamma - \frac{3}{c^2} \partial_\alpha (n u_\alpha u_\beta u_\gamma) \\
&\quad + u_\gamma \partial_\alpha \left(n \delta_{\alpha\beta} - \frac{3}{c^2} P_{\alpha\beta} \right) + u_\beta \partial_\alpha \left(n \delta_{\alpha\gamma} - \frac{3}{c^2} P_{\alpha\gamma} \right) \\
&\quad + (u_\alpha \partial_\alpha n) \partial_n \left(n \delta_{\alpha\beta} - \frac{3}{c^2} P_{\alpha\beta} \right) + (\partial_\alpha u_\alpha) \\
&\quad \times \left(n \delta_{\beta\gamma} - \frac{3}{c^2} n \partial_n P_{\beta\gamma} \right) \Bigg],
\end{aligned} \tag{8}$$

and a convection-diffusion equation for the order parameter

$$\partial_t \phi + \partial_\alpha (\phi u_\alpha) = \left(\tau_g - \frac{1}{2} \right) \Delta t \left[\Gamma \nabla^2 \mu - \partial_\beta \left(\frac{\phi}{n} \partial_\alpha P_{\alpha\beta} \right) \right], \tag{9}$$

where $P_{\alpha\beta}$ is the pressure tensor, $(\tau_g - 1/2)\Delta t \Gamma = M$ is called the mobility coefficient and the dynamic viscosity $\nu = (\tau_f - 1/2) c^2 \Delta t / 3$. In the incompressible limit, the first three terms of Eq. (8) reduce to the usual Navier-Stokes equation

$$\partial_t (n u_\gamma) + \partial_\alpha (n u_\gamma u_\alpha) = -\partial_\alpha P_{\alpha\gamma} + \eta \nabla^2 u_\gamma, \tag{10}$$

and the remaining terms are error terms. On the right hand side of Eq. (9), the first term in square brackets is the usual diffusive term and the second is a small error term.

As in I, the evolution equation (2) is split into a collision step and a streaming step. A new field $g^*_{\sigma i}(\mathbf{x},t)$ is defined by the equation

$$g^*_{\sigma i}(\mathbf{x},t) = g_{\sigma i}(\mathbf{x},t) + \frac{1}{\tau_g} (g^{eq}_{\sigma i} - g_{\sigma i}). \tag{11}$$

The $g^*_{\sigma i}(\mathbf{x},t)$ stream according to

$$g_{\sigma i}(\mathbf{x}, t + \Delta t) = g^*_{\sigma i}(\mathbf{x} - \mathbf{e}_{\sigma i} \Delta t, t). \tag{12}$$

One lattice Boltzmann step is considered to be one collision step and one streaming step at each site.

Thermodynamics of the fluid

The free energy we choose to describe the binary fluid is

$$\Psi = \int \mathrm{d}V \left[\frac{A}{2} \phi^2 + \frac{B}{4} \phi^4 + \frac{\kappa}{2} (\boldsymbol{\nabla} \phi)^2 + nT \ln n \right], \tag{13}$$

where the coefficients A and B determine the properties of the bulk phases, T is the temperature, and the term in κ endows the interfaces with surface tension by penalizing nonuniformities in ϕ.

This choice of free energy leads to a chemical potential

$$\mu = \frac{\delta \Psi}{\delta \phi(x)} = A\phi + B\phi^3 - \kappa \nabla^2 \phi \tag{14}$$

and a pressure tensor

$$\begin{aligned}
P_{\alpha\beta} = &\left(nT + \frac{A}{2} \phi^2 + \frac{3B}{4} \phi^4 - \kappa \phi \nabla^2 \phi - \frac{\kappa}{2} (\boldsymbol{\nabla} \phi)^2 \right) \delta_{\alpha\beta} \\
&+ \kappa (\partial_\alpha \phi)(\partial_\beta \phi).
\end{aligned} \tag{15}$$

We choose $T = c^2/3$ to minimize the error terms in Eq. (8).

For two coexisting phases A must be negative (giving a double well potential) and we restrict ourselves here to the choice $A = -B$ and $B > 0$. Minimization of the free energy with respect to variations in ϕ leads to

$$\mu = A\phi + B\phi^3 - \kappa \nabla^2 \phi = 0. \tag{16}$$

Our choice of $A = -B$ gives two possible bulk solutions: $\phi = 1$ and $\phi = -1$. Equation (16) also allows an interface solution of the form

$$\phi = \tanh \left(\frac{x}{\sqrt{2}\xi} \right), \tag{17}$$

with $\xi (= \sqrt{\kappa/B})$ being the interface width. The surface tension for such an interface is $\sigma = \sqrt{8 \kappa B / 9}$.

III. BOUNDARY CONDITIONS

Wetting boundary conditions at the walls are implemented in a way analogous to Sec. III A of I. Following Cahn, we add a surface term to the free energy

$$\Psi = \int_V \mathrm{d}V \left[\frac{A}{2} \phi^2 + \frac{B}{4} \phi^4 + \frac{\kappa}{2} (\boldsymbol{\nabla} \phi)^2 + nT \ln n \right] - \int_S \mathrm{d}S h \phi_s, \tag{18}$$

where h is the wetting potential and ϕ_s is the value of ϕ on the surface s. Minimizing the free energy gives an equilibrium boundary condition $\kappa \partial_\perp \phi = -h$ on s which we impose on the system. To obtain a given wetting angle θ_w, h is chosen from the relation

$$\Omega \equiv \sqrt{\frac{2}{\kappa B}} h = 2 \, \mathrm{sgn} \left(\frac{\pi}{2} - \theta_w \right) \left[\cos \left(\frac{\alpha}{3} \right) \left\{ 1 - \cos \left(\frac{\alpha}{3} \right) \right\} \right]^{1/2}, \tag{19}$$

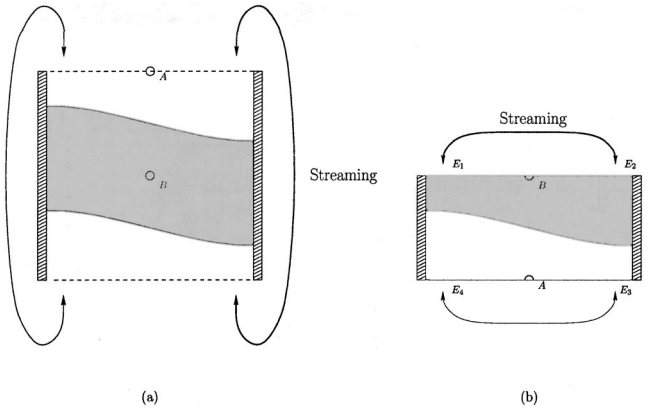

FIG. 1. The effect of streaming with periodic and rotational boundary conditions. (a) Using periodic boundary conditions fluid exits from the top and bottom of the domain and re-enters the system at the bottom and top as indicated by the arrows. There are two rotational symmetry points, *A* and *B*. (b) Using rotational boundary conditions fluid flows between E_1 and E_2 and between E_3 and E_4 under streaming. This use of the symmetry properties in (a) allows the computational burden to be halved.

where $\alpha=\arccos(\sin^2\theta_w)$ and $\mathrm{sgn}(x)$ gives the sign of x [5]. The details of the scheme can be found in Refs. [6] and [7], which show that the correct equilibrium angle is obtained to within 3% for the range $30°<\theta_w<150°$.

To impose shear we use the boundary conditions on the fields $f_{\sigma i}$ described in I, Sec. III B, together with an analogous set of equations for the $g_{\sigma i}$'s. Due to the definition of the boundary conditions L_x, the length of the system in the x direction, equals $(N_x-1)\Delta x$ whereas L_y, the length of the system in the y direction, equals $N_y\Delta x$.

In this paper we will consider periodic boundary conditions in the direction parallel to the shear such that there are two points of rotational symmetry, as shown in Fig. 1(a). In order to reduce the computational burden we can exploit this symmetry as suggested in Fig. 1(b) using ''rotational'' boundary conditions. The details for one lattice site on the row $j=N_y$ are as follows: after the collision step $f^*_{1,2}$, $f^*_{2,1}$, $f^*_{2,2}$, $g^*_{1,2}$, $g^*_{2,1}$ and $g^*_{2,2}$ reside at lattice site (i,N_y). The rotational boundary conditions mean that $f^*_{2,2}$ and $g^*_{2,2}$ stream to $f_{2,4}$ and $g_{2,4}$ at site (N_x-i+1,N_y), $f^*_{1,2}$ and $g^*_{1,2}$ stream to $f_{1,4}$ and $g_{1,4}$ at site (N_x-i,N_y) and $f^*_{2,1}$ and $g^*_{2,1}$ stream to $f_{2,3}$ and $g_{2,3}$ at site (N_x-i-1,N_y). Using rotational boundary conditions means that the domains may be halved in size.

IV. SHEARED SYSTEMS

We consider a system initially in equilibrium with two coexisting phases. Phase 1 ($\phi=-1$) occupies the region $0<x<L_x, -L_y/2<y<0$ and phase 2 ($\phi=+1$) the region $0<x<L_x, 0<y<L_y/2$. The contact angles are 90° and in equilibrium the interface is along the line $y=0$. We impose a shear on the system by moving the walls at $x=0$ and L_x with velocities $+V_0\hat{\mathbf{y}}$ and $-V_0\hat{\mathbf{y}}$. A steady state is achieved as shown in Fig. 2. We measure the angle $\theta(x)$ that the tangent to the interface at x makes with the wall at $y=0$ measured through phase 2.

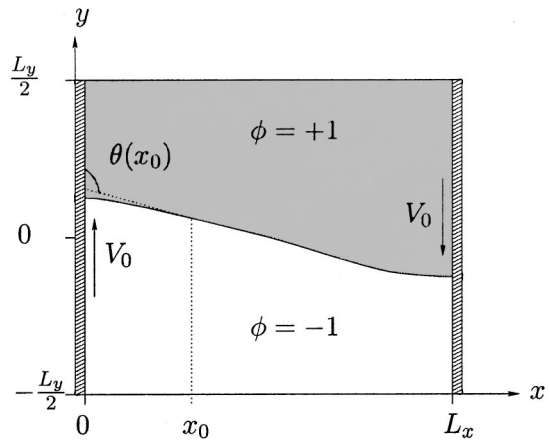

FIG. 2. The steady state of the sheared system showing $\theta(x_0)$, the angle the tangent to the interface at x_0 makes with the wall at $x=0$. V_0 is the speed of the walls.

Interface profiles of systems for increasing shear rates are shown in Fig. 3 and the parameter sets used are given in Table I. The systems approach the static angle ($\theta=90°$) at the walls and achieve a maximum angle in the center. The maximum angle increases with the shear rate. In Fig. 4 we plot the interface curvatures, $\tilde{R}^{-1}(x)$, (normalized to unity) for the systems in Fig. 3 and observe that the normalized profiles collapse onto the same curve. Therefore, we conclude that the wall speed does not affect the curvature profile of the interface, other than to determine its magnitude.

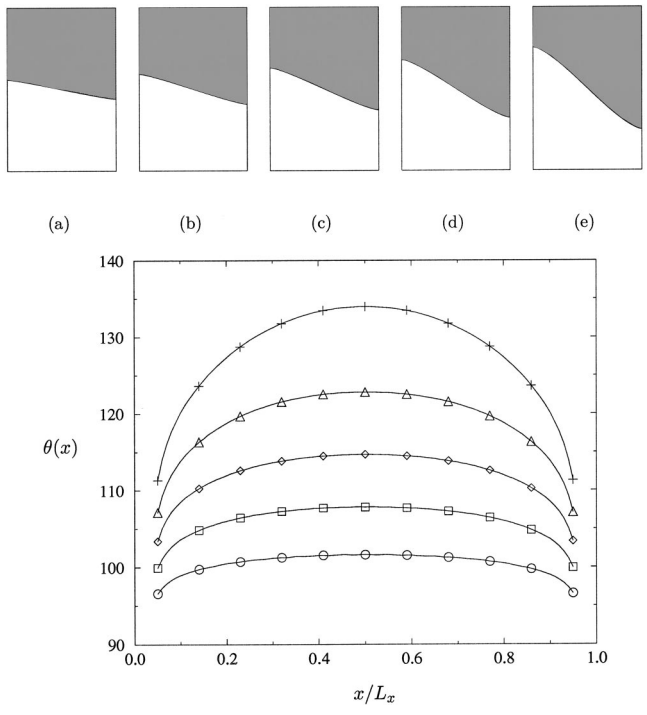

FIG. 3. Top: Real space interface configurations for the simulations described in Table I. Dark shading represents the phase $\phi=+1$ and no shading the phase $\phi=-1$. Bottom: Interface profiles for systems of increasing V_0. The symbols ○, □, ◇, △, and + denote systems a, b, c, d, and e, respectively (see Table I).

TABLE I. Parameter sets for systems with increasing V_0.

System	N_x	N_y	B	τ_f	τ_g	V_0	κ	Γ
a	100	150	0.003	0.8	1.0	0.00050	0.01	8.0
b	100	150	0.003	0.8	1.0	0.00075	0.01	8.0
c	100	150	0.003	0.8	1.0	0.00100	0.01	8.0
d	100	150	0.003	0.8	1.0	0.00125	0.01	8.0
e	100	150	0.003	0.8	1.0	0.00150	0.01	8.0

We now focus on one particular system and study the chemical potential and velocity field in detail. We choose the system in Fig. 3(c).

In equilibrium the chemical potential is zero everywhere, while in the sheared system we expect a nonzero chemical potential. In Fig. 5 we show a three-dimensional plot of the chemical potential for the chosen system. We see that where the interface is in contact with the surface the chemical potential takes its extremal values. The Gibbs-Thompson relation gives the value of the chemical potential at a gently curved interface [8]. It is

$$\mu\Delta\phi=\frac{\sigma}{R}, \tag{20}$$

where σ is the surface tension, $\Delta\phi$ is the difference in the order parameter across the interface and R is the radius of curvature. As a check, we plot both μ and $\sigma/(R\Delta\phi)$ at the curved interface against x on the same axes in Fig. 6. As expected we see that the Gibbs-Thompson relation holds.

In Fig. 7 we plot the fluid velocity near to the contact point at $i=1$ (i.e., $x=0$). We plot both the flow field [Fig. 7(a)] and the normalized flow field [Fig. 7(b)], which shows the flow direction. Near the contact point we see that fluid flows through the interface due to the no slip boundary condition. Note, however, that there is flow through the interface in the opposite direction to this in the region $4\leqslant i\leqslant 9$. Thus, there is a stagnation point in the flow field as the flux through the interface changes direction from positive to negative. For

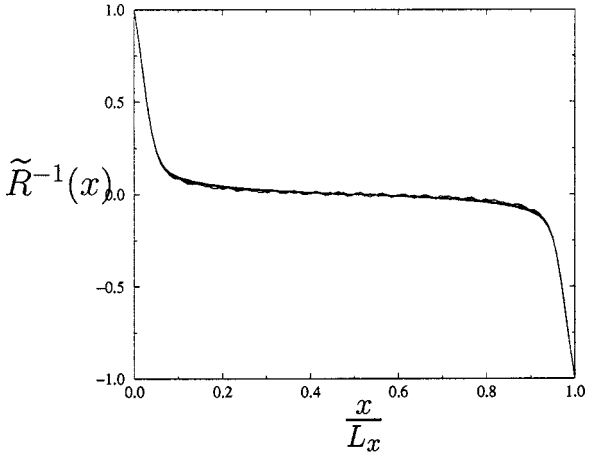

FIG. 4. Interface curvature, $\widetilde{R}^{-1}(x)$, (normalized by its maximum) against x/L_x for the five systems in Fig. 3. Increasing the wall velocity does not affect the length scale of the profiles.

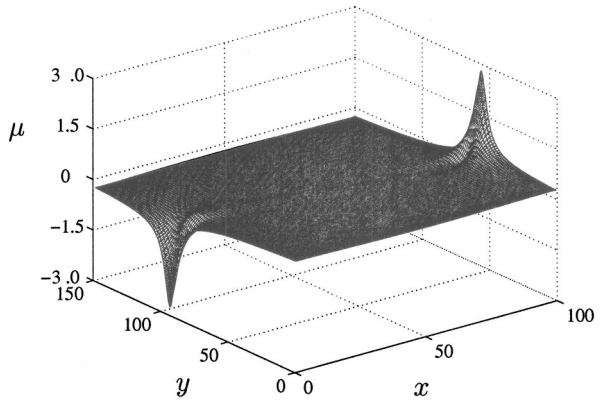

FIG. 5. Three-dimensional plot of the chemical potential μ for system (c) in Table I (the μ axis is scaled by 10^4). The negative and positive peaks occur where the interface is in contact with the surfaces and drive interspecies diffusion.

$10<i<30$ the flow field is parallel to the interface and directed away from the contact point. This region corresponds to the classical solution, where the tangential velocity of the fluids is continuous across the interface. The normalized flow field shows a jet into phase two (dark shading) as expected for the wedge flow solution [9].

In Fig. 8 we plot the fluid velocity in the center of the system, $30<i<70$. [Again, the normalized flow field is shown in Fig. 8(b).] We see that the flow in the interfacial region is very small but in different directions across the interface. We see that in this region the flow is influenced by the jet in phase two (from the contact point at $i=1$) and the jet in phase one (from the contact point at $i=100$). Thus, in this region the flow is geometry dependent and not expected to match the wedge solution. However, in this region, there is still no flow across the interface.

We may therefore consider the flow field near the interface in terms of two different regions: The first, near to the

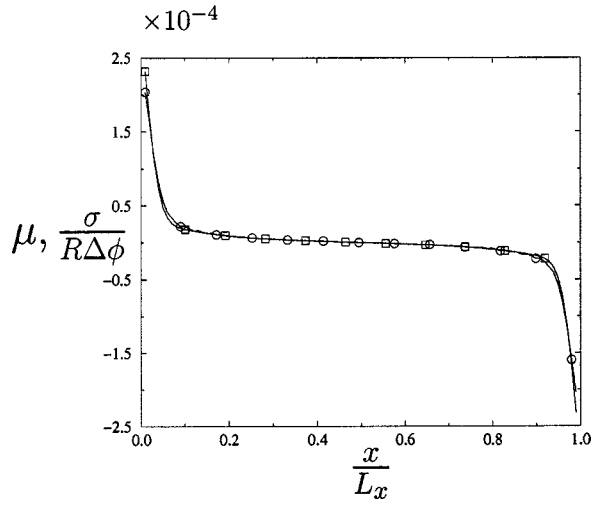

FIG. 6. The two terms of the Gibbs-Thompson relation, Eq. (20), at the interface for system (c) in Table I (□ denotes μ and ○ denotes $\sigma/[R\Delta\phi]$). Diffusive effects are only important in the immediate vicinity of the walls.

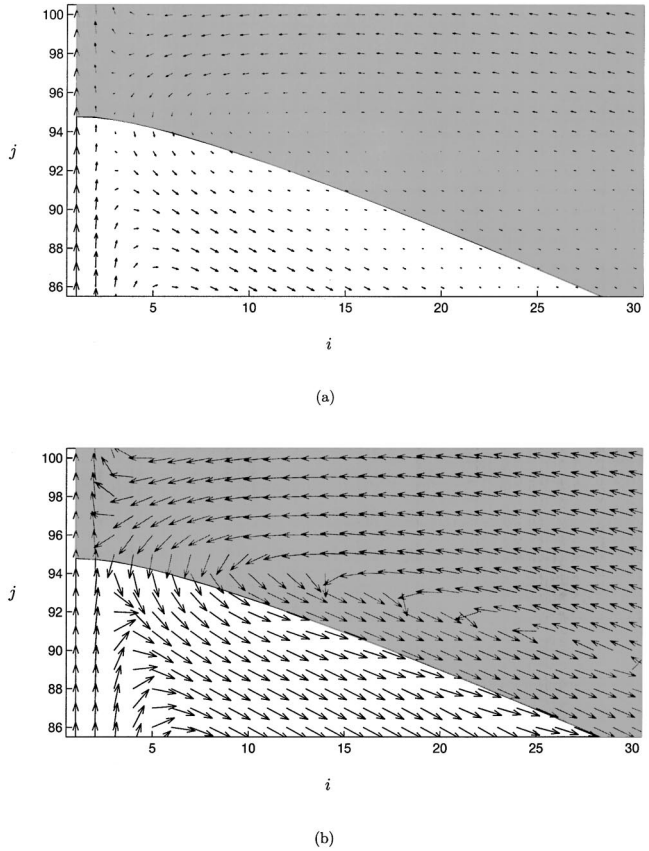

FIG. 7. Fluid velocity plots near the contact point at $i=1$ (i.e. $x=0$). (a) shows the flow field $\mathbf{u}(i,j)$, which has a maximum speed of V_0 along the line $i=1$. (b) shows the normalized flow field $\mathbf{u}(i,j)/|\mathbf{u}(i,j)|$, which displays the flow parallel to the interface and the jet into phase 2. In the region $1<i<10$, there is flow across the interface.

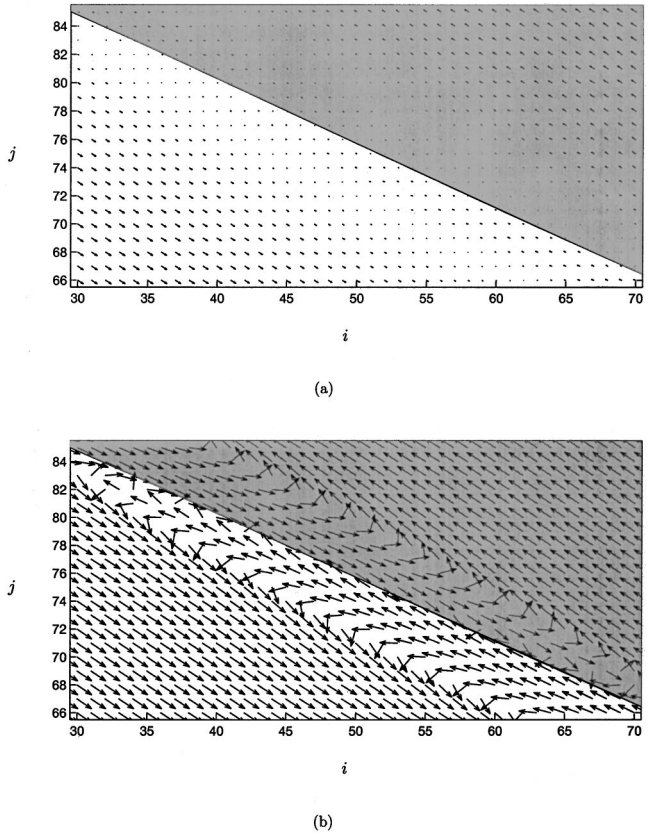

FIG. 8. Fluid velocity plots for the center of the system ($30<i<70$). (a) shows the flow field $\mathbf{u}(i,j)$ on the same scale as Fig. 7(a). (b) shows the normalized flow field $\mathbf{u}(i,j)/|\mathbf{u}(i,j)|$, which exhibits the jets from both contact points. The flow in this region is therefore geometry dependent.

two contact points, has flow across the interface and the second, in the center of the system, has no flow across the interface.

We can make these observations more precise by considering the convection-diffusion equation in the steady state

$$\mathbf{u}\cdot\boldsymbol{\nabla}\phi = M\nabla^2\mu. \tag{21}$$

For flow through the interface (i.e. with a component of $\mathbf{u}$ parallel to $\boldsymbol{\nabla}\phi$) we expect the two sides of the equation to be non-zero and balanced. For flow parallel to the interface (i.e. with $\mathbf{u}$ perpendicular to $\boldsymbol{\nabla}\phi$) we expect both sides of the equation to be zero. In Fig. 9 we plot both terms of the convection-diffusion equation and observe the two different regions. For $0<x/L_x\lesssim 0.1$ and $0.9\lesssim x/L_x<1$ nonzero terms balance while in the rest of the domain both terms are zero. We conclude that diffusion effects are important near to the contact line whereas further away diffusion plays no role.

Clearly it is important to understand the role diffusion plays in allowing the contact line to slip relative to the wall. To this end we propose a measure of how the size of this diffusion region varies with the system parameters. We characterize this size by measuring the distance over which $M\nabla^2\mu$ at the interface (normalized by its value at the wall) falls through zero and rises again to the value -0.1. We call this length L (see Fig. 10).

We varied the system parameters V_0, η, κ and M within the stable ranges of the simulation and measured L. The results are shown on logarithmic plots in Fig. 11 together with straight line fits to determine the exponents, which are listed in Table II. To show the quality of the data we have plotted L against $M^{c_1}\eta^{c_2}\kappa^{c_3}$ for all the data sets in Fig. 12. This shows that our straight line fits are consistent over the complete range of parameters used. For small values of L the fit of the data is worse as lattice effects increase. At the high end of the range, the data is generated using parameters at the edge of computational stability, hence reducing accuracy. The exponents for V_0 and M leads us to conclude that L is indepen-

TABLE II. Values of the exponents (with errors) for the diffusive length scale L. Thus $L\sim M^{c_1}\eta^{c_2}\kappa^{c_3}$ with the values given.

Parameter	Exponent	Value	Error
Velocity, V_0	c_0	0.00	0.00
Mobility, M	c_1	0.25	0.01
Viscosity, η	c_2	0.28	0.01
surface tension parameter, κ	c_3	0.20	0.01

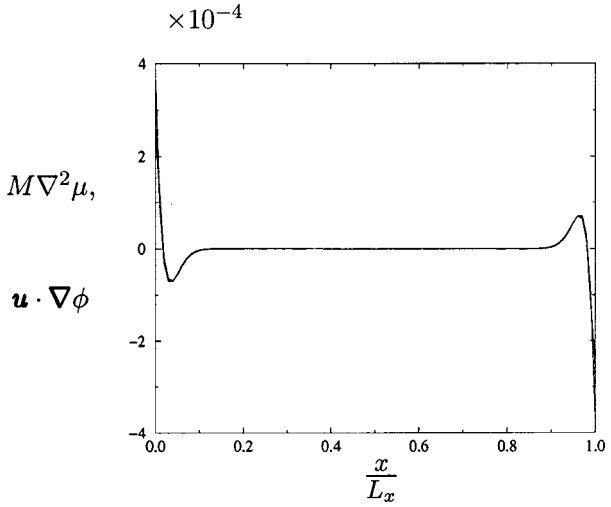

FIG. 9. The two terms of the convection-diffusion relation at the interface. The two curves are almost indistinguishable, hence we show no symbols. Diffusion is evidenced by the flow through the interface, which is only significant near the walls.

dent of V_0 and scales with $M^{1/4}$. The exponents for η and κ are 0.28 and 0.20, which are both consistent with 0.25, given that systematic errors enter the simulation when τ_f and κ are varied. In Sec. V we will argue that the functional form for L is

$$L^{\mathrm{eff}} \sim \left(\frac{\eta M \xi^2}{\Delta \phi^2} \right)^{1/4}, \tag{22}$$

which, recalling that $\xi^2 \sim \kappa$, is consistent with the scaling observed.

V. A SCALING ARGUMENT

To find a scaling form for L^{eff}, we consider how the steady-state Stokes and convection-diffusion equation scale in terms of two length scales, ξ and L. Our argument is that ξ is a static length scale which charaterizes ϕ (the only nontrivial static field) and that a dynamical length scale L characterizes the fields μ and $\mathbf{u}$ (which are nontrivial only in the dynamical case).

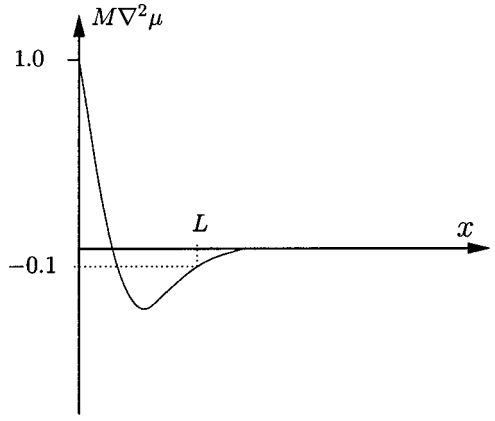

FIG. 10. Definition of L. Note that $M\nabla^2\mu$ is normalized by its value at the wall.

We start by considering the y component of the steady-state Stokes equation for a incompressible fluid [Eq. (10) with the left hand side set to zero], integrated across the interface in the y direction:

$$\int \mathrm{d}y[\partial_x P_{yx} + \partial_y P_{yy}] = \eta \int \mathrm{d}y \nabla^2 u_y . \tag{23}$$

Using the definition of $P_{\alpha\beta}$ and a little algebra we rewrite the left hand side of Eq. (23) as

$$\int \mathrm{d}y \partial_y (nT) + \int \mathrm{d}y \phi \partial_y \mu. \tag{24}$$

The first term is zero for an incompressible fluid. The second term can be integrated by parts to give $[\phi\mu] - \int \mathrm{d}y(\mu \partial_y \phi)$ which scales as $\mu(\Delta\phi/\xi)\xi$.

To find the scaling of the right hand side of Eq. (23) we use L as the length scale for the velocity field. It follows that the scaling is $\eta u_y \xi / L^2$, leaving us with

$$\mu \frac{\Delta\phi}{\xi} \sim \eta \frac{u_y}{L^2}. \tag{25}$$

To determine the form for L we now use the convection-diffusion equation to eliminate μ and u_y from Eq. (25). In the steady state we have

$$\mathbf{u} \cdot \boldsymbol{\nabla} \phi = M \nabla^2 \mu. \tag{26}$$

The scaling length for μ is L and $\boldsymbol{\nabla}\phi$ scales like $\Delta\phi/\xi$. Therefore the convection-diffusion equation scales as

$$u_y \frac{\Delta\phi}{\xi} \sim M \frac{\mu}{L^2}. \tag{27}$$

Multiplying Eqs. (25) and (27) and canceling the factors of μu_y gives

$$\left(\frac{\Delta\phi}{\xi} \right)^2 \sim \frac{\eta M}{L^4}. \tag{28}$$

Finally we conclude that L scales as

$$L \sim \left(\frac{\eta M \xi^2}{\Delta \phi^2} \right)^{1/4}. \tag{29}$$

VI. DISCUSSION

We have performed lattice Boltzmann simulations of contact line motion on a diffuse interface binary system using no slip conditions at the boundary. The stress singularity at the contact line is replaced by a finite peak. We have observed how two distinct regions occur. Far from the contact line the fluid flows parallel to the interface, as for the classical solution, indicating no diffusion. Near the contact line, however, there is a region where fluid flows across the interface which

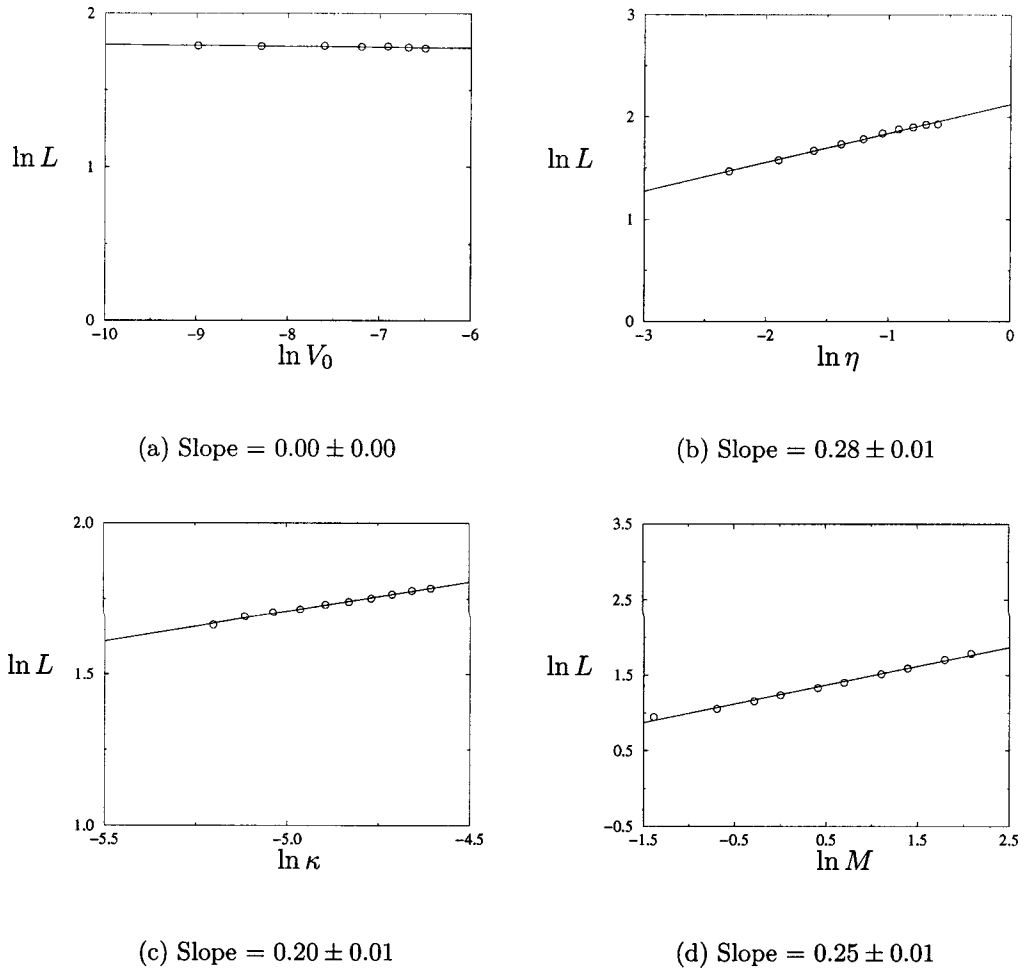

FIG. 11. Straight line fits to determine the dependence of L on simulation parameters. (a) wall velocity V_0, (b) viscocity η, (c) surface tension parameter κ, and (d) mobility M. The exponents are listed in Table II.

signals that diffusive effects are important. We used scaling considerations to argue that this length scales as

$$L \sim \left(\frac{\eta M \xi^2}{\Delta \phi^2} \right)^{1/4}. \tag{30}$$

We have measured the scaling of L with the system parameters V_0, M, η, and κ. Recalling that $\xi \propto \sqrt{\kappa}$, we observe that the results agree well with the scaling argument for V_0 and M (with exponents 0.00 and 0.25, respectively) and that the exponents 0.28 for η and 0.20 for κ are consistent with $\eta^{1/4}$ and $(\xi^2)^{1/4}$. We now compare the results of Secs. IV and V to other work in the literature.

The classical work on contact line motion (treating the fluids as completely immiscible) culminated in the general treatment of Cox [9]. More recently, the contact line problem in binary fluids has been investigated using diffuse interface methods by Jacqmin [2] (using asymptotic analysis and finite difference calculations) and Chen *et al.* [3] (who used an approximate analytical solution and direct numerical solution to the diffuse interface equations). In the remainder of this section we consider these treatments in turn, showing that our data is consistent with Cox's results and highlighting the differences between our conclusions and those of Jacqmin and Chen *et al.* Finally, we discuss the validity of the results in the context of no-slip boundary conditions.

Cox's analysis of the contact line problem treated the

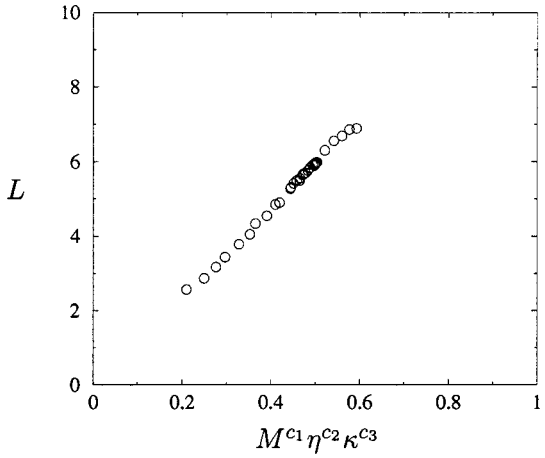

FIG. 12. L from all data sets against $M^{c_1}\eta^{c_2}\kappa^{c_3}$ with the exponents taking the values in Table II.

fluid-fluid interface as a material boundary so the two fluids could not mix. At the wall the singularity in the stress was relaxed by allowing the fluid to slip at distances of order s from the contact point. Three different phenomenological slip models were used. Cox's analysis was performed using matched asymptotic expansions in two small parameters ($\epsilon = s/R$, where R was a macroscopic length scale, and Ca the capillary number). It was found that two or three regions of expansion were required.

The outer region solution for the interface shape and flow field depended on the of the system under consideration. The inner region solution for the interface shape and flow field depended on the slip model used. These two solutions were matched by joining the asymptotic form for the interface profile in the inner region as $r \to \infty$ to that of the outer region as $\epsilon \to 0$. In the most general case an intermediate region was required to perform this matching procedure.

The result for the asymptotic form of the interface profile of the inner region as $r \to \infty$, to lowest order in Ca and ϵ was

$$\theta(r) = \theta_0 + Ca\left\{ f(\theta_0,\lambda)\ln r + f(\theta_0,\lambda)\ln\left(\frac{R}{s}\right) + Q_i^* \right\}, \tag{31}$$

where θ_0 is the angle of the interface at its intersection with the wall, r is the distance between the contact point and a point on the interface, R is a characteristic macroscopic length, λ is the viscosity ratio of the two fluids, Q_i^* is a constant of integration dependent on the slip model used and

$$f(\theta,\lambda) = \frac{2\sin\theta[\lambda^2(\theta^2-\sin^2\theta) + 2\lambda\{\theta(\pi-\theta)+\sin^2\theta\} + \{(\pi-\theta)^2-\sin^2\theta\}]}{\lambda(\theta^2-\sin^2\theta)\{(\pi-\theta)+\sin\theta\cos\theta\} + \{(\pi-\theta)^2-\sin^2\theta\}(\theta-\sin\theta\cos\theta)}. \tag{32}$$

To compare Eq. (31) to the simulation results we plot, in Fig. 13, $\ln r$ against $\theta(r)$ for the systems in Fig. 3. We expect that the lattice Boltzmann interfaces obey Cox's solution in the region where tangential velocity is continuous across the interface [identified in Fig. 7(b)]. In Fig. 13 this corresponds to $2.3 \lesssim \ln r \lesssim 3.4$, where all five interfaces are consistent with $\theta(r) \propto \ln r$. Furthermore, in this linear region the slope of $\theta(r)$ with $\ln r$ increases with increasing V_0, as expected from Eq. (31). Thus we have demonstrated the compatibility of the our data with the classical two-fluid treatment.

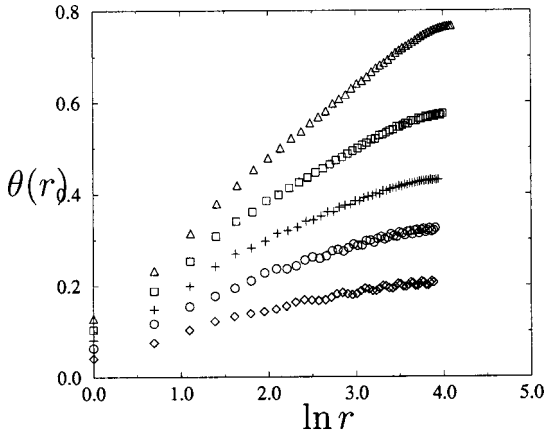

FIG. 13. $\theta(r)$ vs $\ln r$ for the five systems of Fig. 3 (The symbols ◇, ○, +, □, and △ denote systems a, b, c, d, and e of Table I, respectively.) In the region where flow is expected to match the classical slip solution ($2.3 \lesssim \ln r \lesssim 3.4$) θ increases linearly with $\ln r$ [corresponding to the $\ln r$ term in Eq. (31)]. As the capillary number increases the slope of the plot in this region increases, as expected from the factor of Ca in Eq. (31). Therefore we conclude that outside the diffusive region the interface behavior is consistent with the classical solution [9].

In the first study of the diffuse interface binary system applied to contact line motion, Jacqmin [2] identified a length scale for the chemical potential and claimed that this scales as $\sqrt{\eta M}$ ($\Delta\phi = 1$ in Jacqmin's work). The length-scale put forward by Jacqmin differs in form from Eq. (29), and is not supported by our data. Studying the same system as in Sec. IV, Jacqmin noted that the chemical potential patterns "roughly halves in size" between data sets in which ξ (and M) decreases by a factor of four. However, there is no quantitative analysis supporting the form used for the length-scale.

The work of Chen *et al.* [3] suggests a length scale, $l_0 = \sqrt{(2M\sigma/V_0(\Delta\phi)^2)}$, which is $\sqrt{2\sigma/(\eta V_0)}$ times the length scale proposed by Jacqmin. Significantly this length scale diverges as $V_0 \to 0$, a phenomenon we do not observe. In Ref. [3], no direct measurement of a length scale is discussed. The identification of l_0 comes from scaling the convection-diffusion equation, treating μ and ϕ as having the same length scale. This suggests that in the region near to the contact point the interface no longer has it static width ξ. However, our data indicates that, at least for the moderate shear rates considered here, the scale of the interface remains determined by equilibrium properties. The flow field u and chemical potential μ are only nonzero in the moving system and so their length scale is set by the size of the diffusive region.

We have shown how a diffuse interface model can overcome the contact line problem, even under strict no-slip conditions. However an effective slip length, introduced by diffusive effects, gives the same macroscopic interface behavior as a slip boundary condition. To pinpoint the physically relevant mechanism, which may well be system dependent, nanoscale experiments or extremely large molecular dynamics simulations will be needed.

ACKNOWLEDGMENTS

We thank C. Denniston and M. Robbins for helpful discussions. A.B. acknowledges EPSRC research studentship 99315535 and a CASE award from Unilever plc.

APPENDIX: COEFFICIENTS FOR THE BINARY MODEL

The coefficients are

$$A_2=\frac{Tr(P_{\alpha\beta})}{24}, \tag{A1}$$

$$A_1=4A_2, \quad A_0=n-20A_2, \tag{A2}$$

$$B_2=\frac{n}{12}, \quad B_1=4B_2, \tag{A3}$$

$$C_2=-\frac{n}{24}, \quad C_1=4C_2, \quad C_0=16C_2, \tag{A4}$$

$$D_2=\frac{n}{8}, \quad D_1=4D_2, \tag{A5}$$

$$G_{2xx}=\frac{p}{8}+\frac{\kappa}{8}(\partial_x\phi)^2-\frac{Tr(P_{\alpha\beta})}{16}, \tag{A6}$$

$$G_{2xy}=G_{2yx}=\frac{\kappa}{8}[(\partial_x\phi)(\partial_y\phi)], \tag{A7}$$

$$G_{2yy}=\frac{p}{8}+\frac{\kappa}{8}(\partial_y\phi)^2-\frac{Tr(P_{\alpha\beta})}{16}, \tag{A8}$$

$$G_{1\alpha\beta}=4G_{2\alpha\beta} \quad \text{for all} \quad \alpha,\beta, \tag{A9}$$

$$H_2=\frac{\Gamma\mu}{12}, \quad H_1=4H_2, \quad H_0=\phi-20H_2, \tag{A10}$$

$$K_2=\frac{\phi}{12}, \quad K_1=4K_2, \tag{A11}$$

$$J_2=-\frac{\phi}{24}, \quad J_1=4J_2, \quad J_0=16J_2, \tag{A12}$$

$$Q_2=\frac{\phi}{8}, \quad Q_1=4Q_2. \tag{A13}$$

[1] A. J. Briant, A. J. Wagner, and J. M. Yeomans Phys. Rev. E **69**, 031602 (2004).
[2] D. Jacqmin, J. Fluid Mech. **402**, 57 (2000).
[3] H.-Y. Chen, D. Jasnow, and J. Viñals, Phys. Rev. Lett. **85**, 1686 (2000).
[4] A. J. Wagner, D. Phil. thesis, University of Oxford, 1997.
[5] P. Papatzacos, Transport Porous Media **49**, 139 (2002).
[6] A.J. Briant, P. Papatzacos, and J.M. Yeomans, Philos. Trans. R. Soc. London, Ser. A **360**, 485 (2002).
[7] A. J. Briant, D. Phil. thesis, University of Oxford, 2003.
[8] A.J. Bray, Adv. Phys. **43**, 357 (1994).
[9] R.G. Cox, J. Fluid Mech. **168**, 169 (1986).